ACS Electrochemistry

pubs.acs.org/electrochem Article

Ultrafast High-Capacity Calcium-Ion Battery Based on Efficient Calciation into the Two-Dimensional Structure of a Cu_3(2,3,6,7,10,11-hexahydroxytriphenylene)$_2$ Cathode

Katsuhiro Wakamatsu,[‡] Shunsuke Ohkata,[‡] Mizuki Kajiwara, Naoki Tanifuji, Hirofumi Yoshikawa,* and Takeshi Shimizu*

Cite This: *ACS Electrochem.* 2026, 2, 596−603

Read Online

ACCESS | Metrics & More | Article Recommendations | Supporting Information

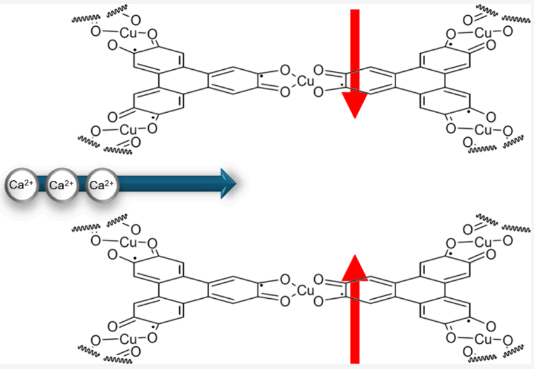

ABSTRACT: Calcium-ion batteries (CIBs) are promising energy storage systems because of their low cost and high theoretical volumetric energy density. However, calcium ion (Ca^{2+}), a divalent cation with a larger ionic radius than lithium ion, forms strong electrostatic interactions with the divalent O^{2-} anion in conventional metal-oxide-based cathode active materials, resulting in capacities less than 55% of the theoretical values and poor rate performance. In this study, $Cu_3(HHTP)_2$ (HHTP: 2,3,6,7,10,11-hexahydroxytriphenylene), a two-dimensional metal-organic framework with monovalent O^- anions included in its crystal structure, is used as a cathode active material for CIBs, and its performance, as well as its calciation and de-calciation mechanisms, is investigated. $Cu_3(HHTP)_2$ has a high initial capacity equal to 86% of the theoretical value and excellent rate performance owing to sufficient redox reaction and smooth calciation, respectively. However, it exhibits poor cycle performance because of insufficient de-calciation during charging, which results from electrostatic interactions between intercalated Ca^{2+} ions with O^- anions in the narrower interlayer spacing of $Cu_3(HHTP)_2$ after the first discharge. These findings provide valuable insights for improving the performance of cathode active materials for CIBs.

KEYWORDS: *calcium-ion battery, metal-organic framework, monovalent anion, cathode active material, two-dimensional crystal structure, calciation, de-calciation*

INTRODUCTION

Rechargeable batteries are effective energy storage systems that provide portable and renewable power. In particular, lithium-ion batteries (LIBs) have been used as an energy source for various portable devices, such as mobile phones and laptops, since the 1990s.[1] In conventional LIBs composed of a metal-oxide-based cathode ($LiCoO_2$), graphite (C) anode, and liquid-state electrolyte with lithium ions (Li^+), a reversible redox reaction occurs during discharging and charging according to eqs 1−3.

Cathode:

$$LiCoO_2 \rightleftarrows Li_{1-x}CoO_2 + xLi^+ + xe^- \tag{1}$$

Anode:

$$6C + Li^+ + e^- \rightleftarrows LiC_6 \tag{2}$$

Total:

$$LiCoO_2 + 6xC \rightleftarrows Li_{1-x}CoO_2 + xLiC_6 \tag{3}$$

As indicated in eq 3, Li^+ ions reversibly migrate as carrier ions from the $LiCoO_2$ cathode to the graphite anode through the electrolyte during charging.[2] The opposite reaction occurs during discharging,[2] achieving reversible conversion between chemical and electrical energies. Recently, alternative carrier ions, such as sodium (Na^+),[3] zinc (Zn^{2+}),[4] and calcium (Ca^{2+}),[5,6] have been used to develop high-performance, low-cost rechargeable batteries. In particular, calcium-ion batteries (CIBs) have been investigated because of their very low cost (2.28 USD kg^{-1}),[7] high theoretical volumetric energy density based on a relatively low potential of −2.88 V vs. standard hydrogen electrode (SHE) (Li^+/Li: −3.01 V vs. SHE), and calciation of active materials.[5,6] However, calciation into metal-oxide-based cathode active materials is a difficult process because of two reasons: First, intercalation of Ca^{2+}, which has a larger ionic radius (1.00 Å) than Li^+ (0.76 Å),[8] into the

Received: June 14, 2025
Revised: January 15, 2026
Accepted: January 22, 2026
Published: January 28, 2026

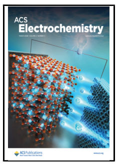

https://doi.org/10.1021/acselectrochem.5c00241
ACS Electrochem. 2026, 2, 596−603

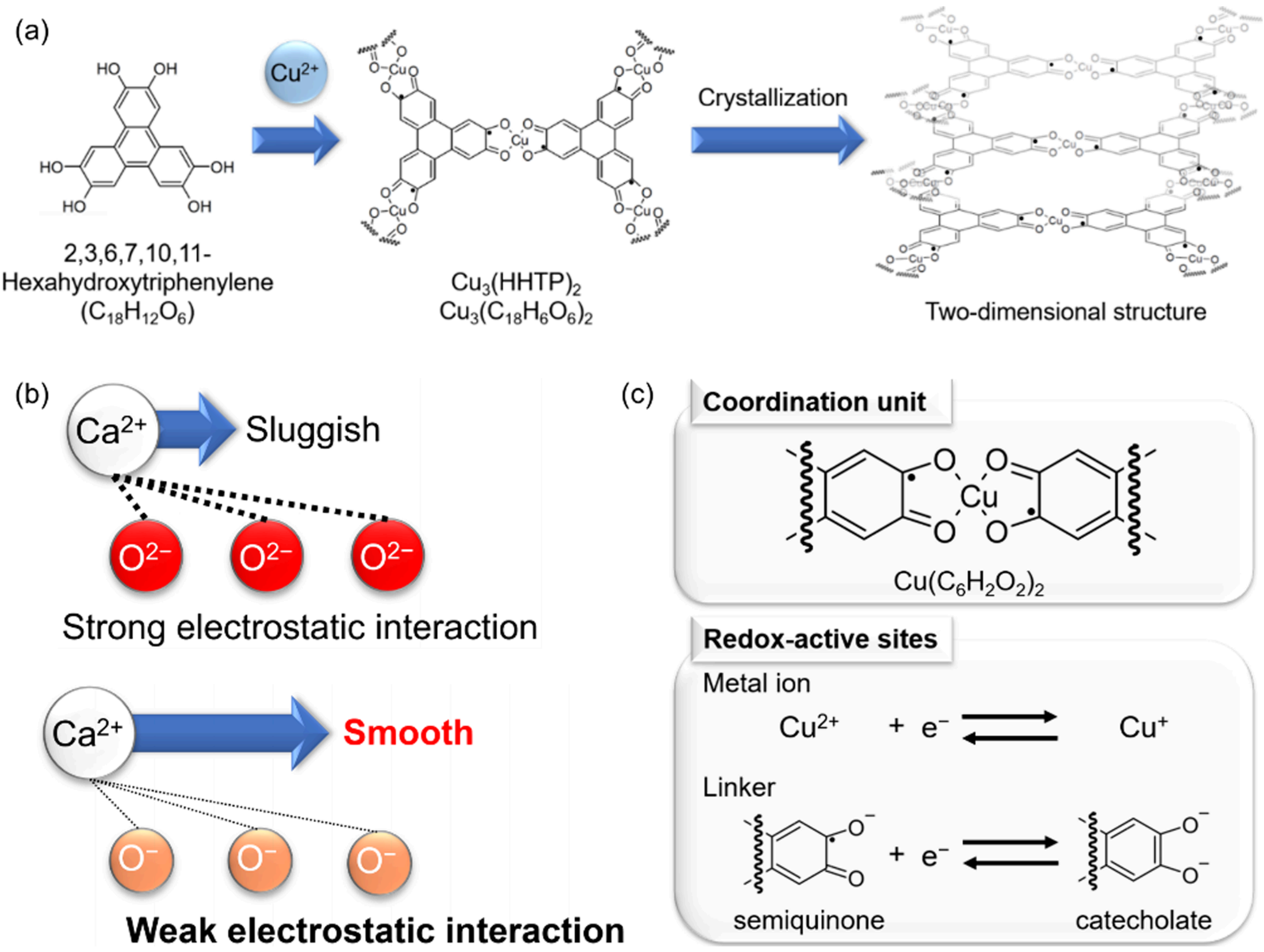

Figure 1. (a) Crystal structure of $Cu_3(HHTP)_2$. (b) Schematic illustration of the electrostatic interactions of Ca^{2+} with divalent O^{2-} and monovalent O^- anions in the crystal structure during calciation. (c) Expected redox reactions of the metal and linker in the coordination unit of $Cu_3(HHTP)_2$.

angstrom-sized space of the metal oxide causes electrode failure.[5] Second, confinement of Ca^{2+} in the crystal structure of the metal oxide through strong electrostatic interactions with O^{2-} hinders its intercalation,[9] resulting in capacities less than 55% of the theoretical values[10−13] and low rate performance[14−18] (Table S1). Moreover, recent cathode active materials also have suffered from low capacity[19,20] and rate performance.[21] Thus, the crystal structure of cathode active materials for CIBs must have a large space and low-valent anions.

Two-dimensional (2D) metal-organic frameworks (MOFs), which are nanoporous crystalline materials composed of metal ions and linkers, exhibit these desirable features. They have been used as cathode active materials for LIBs[22−24] and sodium-ion batteries[25−28] because of their nanosized spaces and redox-active sites (metal ions and linkers). Moreover, MOFs, such as Mg-MOF-74,[29] MIL-101 (Cr),[30] and MOF-688,[31] are excellent quasi-solid-state magnesium ion (Mg^{2+}) conductors because their nanosized channels can improve the conductivity of divalent cations. Recently, 2D MOFs have been used as cathode active materials for rechargeable batteries because their planar $d-\pi$ conjugation and large spaces enhance electronic and ionic conductivities, resulting in excellent battery performance.[32] For example, as cathode active materials for LIBs, $Cu_3(HIB)_2$ (HIB: hexaiminobenzene) and $Cu_3(THQ)_2$ (THQ: tetrahydroxy-1,4-benzoquinone) exhibit high capacities of 200[33] and 340 mAh g^{-1},[34] respectively. $Cu_3(HHTP)_2$ (HHTP: 2,3,6,7,10,11-hexahydroxytriphenylene; Figure 1a) has been used as a cathode active material for high-capacity zinc-ion (Zn^{2+}) batteries (228 mAh g^{-1}).[35] This excellent performance results from the redox reactions of Cu^{2+}/Cu^+ and semiquinone anion radical ($C_6H_2O_2^{\bullet-}$)/catecholate ($C_6H_2O_2^{2-}$), accompanied by intercalation of carrier ions into the large spaces of the MOF.

Considering the large interlayer distance in the crystal structure of $Cu_3(HHTP)_2$ (3.26 Å) that can accommodate Ca^{2+} and presumably weaker electrostatic interactions of its monovalent O^- anions with Ca^{2+} (Figure 1b), $Cu_3(HHTP)_2$ was employed as a cathode active material for CIBs and investigated its performance, as well as its calciation and de-calciation mechanisms. The performance of $Cu_3(HHTP)_2$ was evaluated in terms of its theoretical capacity calculated based on three coordination units of $Cu(C_6H_2O_2)_2$ composed of Cu^{2+} and two semiquinone linkers.[36] As shown in Figure 1c, the number of electrons per coordination unit is three because of the redox reactions of Cu^{2+}/Cu^+ ($1e^- \times 1$) and $C_6H_2O_2^{\bullet-}/C_6H_2O_2^{2-}$ ($1e^- \times 2$), resulting in a total of $n = 9$ electrons per formula unit of $Cu_3(HHTP)_2$. The theoretical capacity can be calculated using eq 4:

$$\text{theoretical capacity} = \frac{1000}{3600}\frac{F}{M_w}n \tag{4}$$

where F (= 96,485 C mol^{-1}) is the Faraday constant and M_w (= 827 g mol^{-1}) is the molecular weight of $Cu_3(HHTP)_2$. A value of 291 mAh g^{-1} was obtained and used to estimate the utilization rate of $Cu_3(HHTP)_2$. The calciation and de-calciation mechanisms of $Cu_3(HHTP)_2$ in CIBs were determined by monitoring the changes in the valence of Cu, crystal structure, and molar ratio of Ca to Cu by X-ray absorption fine structure (XAFS) spectroscopy, powder X-ray diffraction (PXRD), and energy-dispersive X-ray spectroscopy (EDX), respectively.

RESULTS AND DISCUSSION

Characterization

$Cu_3(HHTP)_2$ was synthesized using a previously reported method[37] and characterized by PXRD (Cu Kα, λ = 1.5418 Å) and scanning electron microscopy (SEM). The PXRD pattern exhibited sharp peaks at 2θ = 9.64, 12.86, and 27.78° (Figure 2 and Table S2), which are assigned to the (220), (310), and (001) indexes of rod-like $Cu_3(HHTP)_2$, respectively. The interlayer distance estimated from the (001) index using the Bragg equation was 3.211 Å.[38] Additionally, the SEM image revealed the rod-like morphology of $Cu_3(HHTP)_2$ (Figure S1a−d, Supporting Information). These results suggest that $Cu_3(HHTP)_2$ forms a rod-like crystal structure.[36]

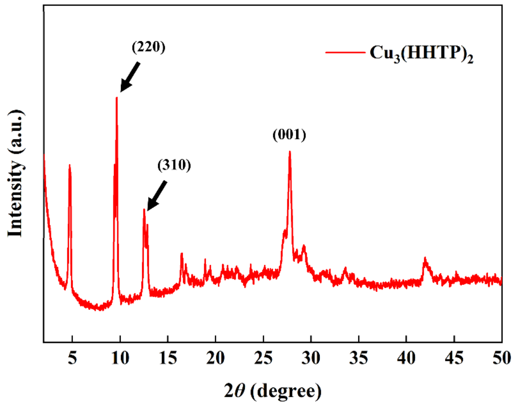

Figure 2. PXRD pattern of $Cu_3(HHTP)_2$.

Battery Performance

For the battery performance tests, the voltage was determined from the cyclic voltammograms of $Cu_3(HHTP)_2$ (Figure 3a). In the first cycle, a pair of redox peaks were observed at −0.7 and 0 V, consistent with the previous result for an LIB with a $Cu_3(HHTP)_2$ cathode (2.2 and 2.7 V vs. Li/Li^+).[36] This suggests that the appropriate voltage for evaluating the performance of $Cu_3(HHTP)_2$ as a cathode active material for CIBs can be determined, that Ca^{2+} can be intercalated into the $Cu_3(HHTP)_2$ crystal structure, and that $Cu_3(HHTP)_2$ undergoes the redox reactions of Cu^+/Cu^{2+} and $C_6H_2O_2^{\bullet-}/C_6H_2O_2^{2-}$. In the second cycle, these redox peaks shifted to higher voltages (voltage range: 0−1.5 V). In contrast, for the aforementioned LIB, the peak intensities of the redox pairs at 2.2/2.7 and 3.2/3.25 V vs. Li/Li^+ decreased and increased gradually, respectively, after the second cycle.[36] This indicates that the mechanism of calciation into $Cu_3(HHTP)_2$ is different from that of lithiation.

The battery performance of the $Cu_3(HHTP)_2$ cathode was evaluated by performing galvanostatic discharge−charge measurements. Herein, CR2032 coin-type cells were assembled using the thin-film cathode, composed of $Cu_3(HHTP)_2$ (30 wt %), carbon black (60 wt %), carboxy methyl cellulose (CMC, 10 wt %), pellet anode, composed of carbon black (80 wt %) and polyacrylonitrile (PAN, 20 wt %), glass microfiber filter separator, and 0.45 M $Ca(BF_4)_2$ in ethylene carbonate/propylene carbonate (1:1 v/v) in an Ar-filled glovebox; they were used to calculate the capacities during 100 cycles and at 50, 100, 500, and 1000 mA g^{-1}. Figure 3b shows that $Cu_3(HHTP)_2$ exhibited a high initial capacity of 250 mAh g^{-1}, which is approximately 86% of the theoretical value (291 mAh g^{-1}) and higher than those of metal-oxide-based cathodes (Table S1). In addition, a long plateau at −0.5 V, corresponding to the reduction peak observed in the cyclic voltammogram (Figure 3a), was observed in the first discharge. This suggests that the initial capacity of $Cu_3(HHTP)_2$ is due to the redox reactions of Cu^+/Cu^{2+} and $C_6H_2O_2^{\bullet-}/C_6H_2O_2^{2-}$. Furthermore, $Cu_3(HHTP)_2$ exhibited a capacity of 70 mAh g^{-1} even at 1000 mA g^{-1} (Figure 3c), indicating that Ca^{2+} can intercalate smoothly into the 2D MOF structure containing monovalent O^- anions. However, the second capacity drastically decreased to 175 mAh g^{-1}, and the first Coulombic efficiency was very low (58%) because of cathode electrolyte interfaces[35] at 100 mA g^{-1} (Figure 3b and Figure 3d, respectively). In addition, the capacity of carbon was not negligible after 10th cycles (Figure S2) and the capacity retention was 37% after 100 cycles at 100 mA g^{-1}, which is and lower than those of CIBs with metal-oxide-based cathodes (Figure 3d and Table S1). The low redox stability of $Cu_3(HHTP)_2$ suggests that de-calciation from the 2D MOF structure is insufficient at low current densities.

DISCHARGE−CHARGE MECHANISM OF $CU_3(HHTP)_2$ IN CIBS

To obtain detailed data on the calciation mechanism, the $Cu_3(HHTP)_2$ cathode in a CIB was investigated by operando Cu K-edge XAFS spectroscopy, ex situ PXRD, and ex situ EDX mapping analysis. The operando Cu K-edge X-ray absorption near-edge structure (XANES) spectra (Figure 4a) showed the valence changes of Cu in $Cu_3(HHTP)_2$. In the initial state, no definite peak was observed in the range of 8980−8990 eV, indicating that the valence of Cu in $Cu_3(HHTP)_2$ was 2+ (Cu^{2+}). In the first discharge state, the shoulder peak assigned to Cu^+[39] was observed at 8980 eV. Although the intensity of this peak decreased during charging, the spectrum did not return to the initial one. In the second discharge state, the spectrum was similar to that in the first discharge state. The spectral change indicates that reduction ($Cu^{2+}\rightarrow Cu^+$) and partial oxidation ($Cu^+\rightarrow Cu^{2+}$) occurred during discharging and charging, respectively. Moreover, X-ray photoelectron spectroscopy measurements confirmed peak shifts of C 1s and O 1s in the cathode. This suggests that the redox reaction of the ligand also occurred (Figure S3). On the other hand, the peak at 28.31° in the PXRD pattern, assigned to (001) of the $Cu_3(HHTP)_2$ crystal structure, shifted to higher and lower values after discharging and charging, respectively (Figure 4b). The interlayer distance changed from 3.152 to 3.048 Å in the first discharge, from 3.048 to 3.102 Å in the first charge, and

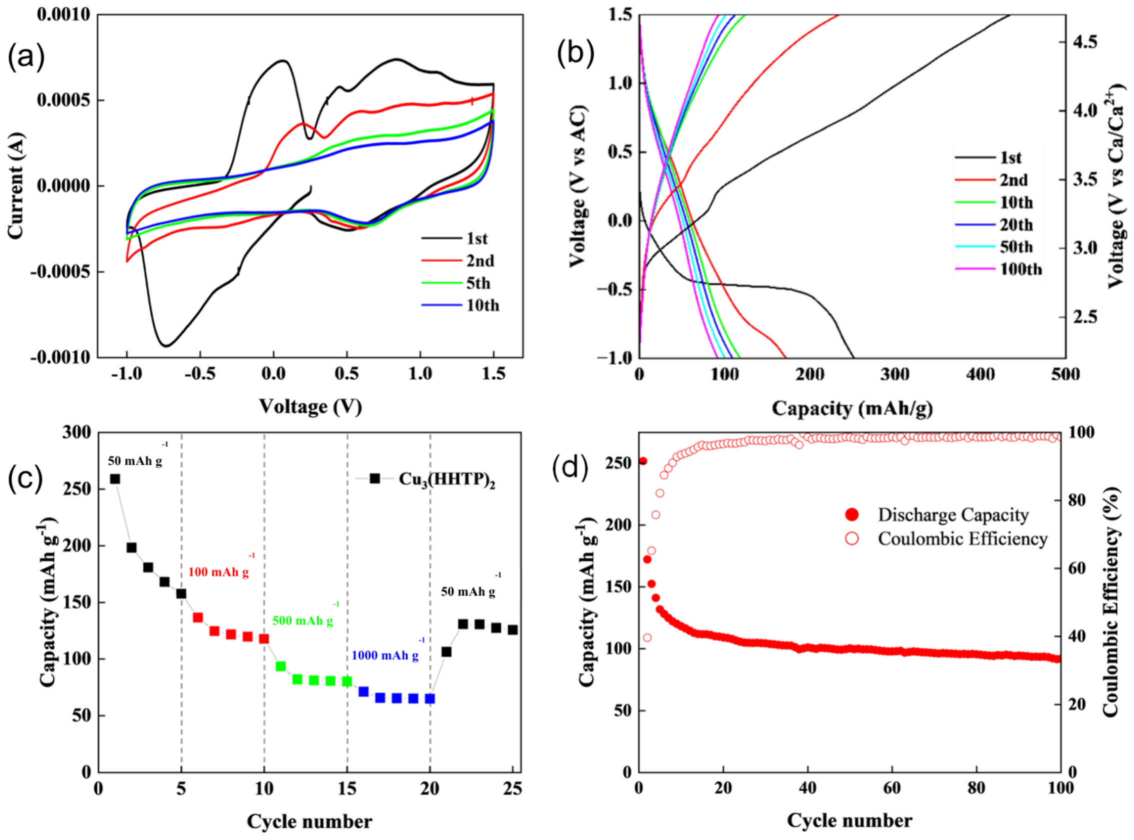

Figure 3. (a) Cyclic voltammograms of a CIB with a $Cu_3(HHTP)_2$ cathode. Voltage: −1.0−1.5 V vs AC, scan rate: 0.2 mV s^{-1}. (b) Discharge−charge curves of $Cu_3(HHTP)_2$. Voltage: −1.0−1.5 V vs AC (approximately 2.3−4.8 V vs Ca/Ca^{2+}), current density: 100 mA g^{-1}. (c) Rate performance of $Cu_3(HHTP)_2$. Current density: 50, 100, 500, and 1000 mA g^{-1}. (d) Cycle performance of $Cu_3(HHTP)_2$. Current density: 100 mA g^{-1}.

from 3.102 to 3.073 Å in the second discharge. This phenomenon is similar to Zn^{2+} intercalation and de-intercalation[35] but different from lithiation (volume expansion) and de-lithiation (shrinkage).[36] This indicates that the career cations with higher valence electrostatically interacted with anions in cathode active materials. A slight peak shift, presumably attributable to Ca^{2+} de-intercalation (a decrease in interlayer distance during discharge and an increase during charging), was also observed in the 10th discharge and charge. Although the peak shift was smaller than in the initial cycles, similar behavior persisted in the 11th cycle, demonstrating a stable and reversible phase change. The limited peak shift indicates that Ca^{2+} de-intercalation from $Cu_3(HHTP)_2$ is minimal, resulting in a non-negligible capacity contribution from carbon black after 10 cycles. Moreover, EDX mapping showed that although Ca was not initially present in the ex situ $Cu_3(HHTP)_2$ pellet cathode (Figure S4a,b), it was detected in the first discharge state (Figure S4c,d). In the first charge state, the ratio of Ca to Cu in the cathode decreased although Ca was still detected (Figure S4e,f). However, in the second discharge state, the ratio of Ca to Cu in the cathode increased (Figure S4g,h and Table S3). Additionally, this tendency could be observed in inductively coupled plasma-mass spectroscopy measurements (Figure S5).

All of these analyses provide the following findings (Figure 4c): Ca^{2+} ions can be sufficiently inserted into the interlayer space of $Cu_3(HHTP)_2$, concurrent with both redox reactions (Cu^{2+}/Cu^{+} and $C_6H_2O_2^{\bullet-}/C_6H_2O_2^{2-}$) in the first discharge state. However, de-calciation from $Cu_3(HHTP)_2$ is insufficient in the first charge state because the intercalated Ca^{2+} ions (ionic radius: 1.0 Å), which are larger than Mg^{2+} (0.728 Å) and Zn^{2+} (0.736 Å),[8] are confined in the narrower 2D space (3.037 Å) of $Cu_3(HHTP)_2$ in the first discharge state owing to strong electrostatic interactions with O^- anions.[32] Consequently, in the second discharge state, a smaller amount of Ca^{2+} ions is intercalated into the narrower interlayer space of $Cu_3(HHTP)_2$ than in the first discharge state. Therefore, the high initial capacity and drastic capacity decay of $Cu_3(HHTP)_2$ can be attributed to sufficient calciation into $Cu_3(HHTP)_2$ in the first discharge state and insufficient de-calciation from $Cu_3(HHTP)_2$ in the subsequent charge state, respectively. Although irreversible capacity due to solid electrolyte interface was small (Figure S5), the solubility of $Cu_3(HHTP)_2$ in the electrolyte also caused the capacity decay (Figure S6).

■ CONCLUSIONS

$Cu_3(HHTP)_2$, a 2D MOF with an ordered crystal structure containing monovalent O^-, was used as a cathode active material for CIBs. It exhibited a high initial capacity of 250 mAh g^{-1} at a low current density of 100 mA g^{-1} and reduced capacity of 70 mAh g^{-1} at a high current density of 1000 mA g^{-1}. This can be attributed to the redox reactions (Cu^{2+}/Cu^{+} and $C_6H_2O_2^{\bullet-}$/ $C_6H_2O_2^{2-}$) and smoother calciation of Ca^{2+} into the crystal structure containing monovalent O^- anions compared with that containing divalent O^{2-} anions. However, $Cu_3(HHTP)_2$ exhibited a low capacity retention of 37% after 100 cycles because of electrostatic interactions between Ca^{2+} ions and the monovalent O^- anions in a narrower space than

https://doi.org/10.1021/acselectrochem.5c00241
ACS Electrochem. 2026, 2, 596−603

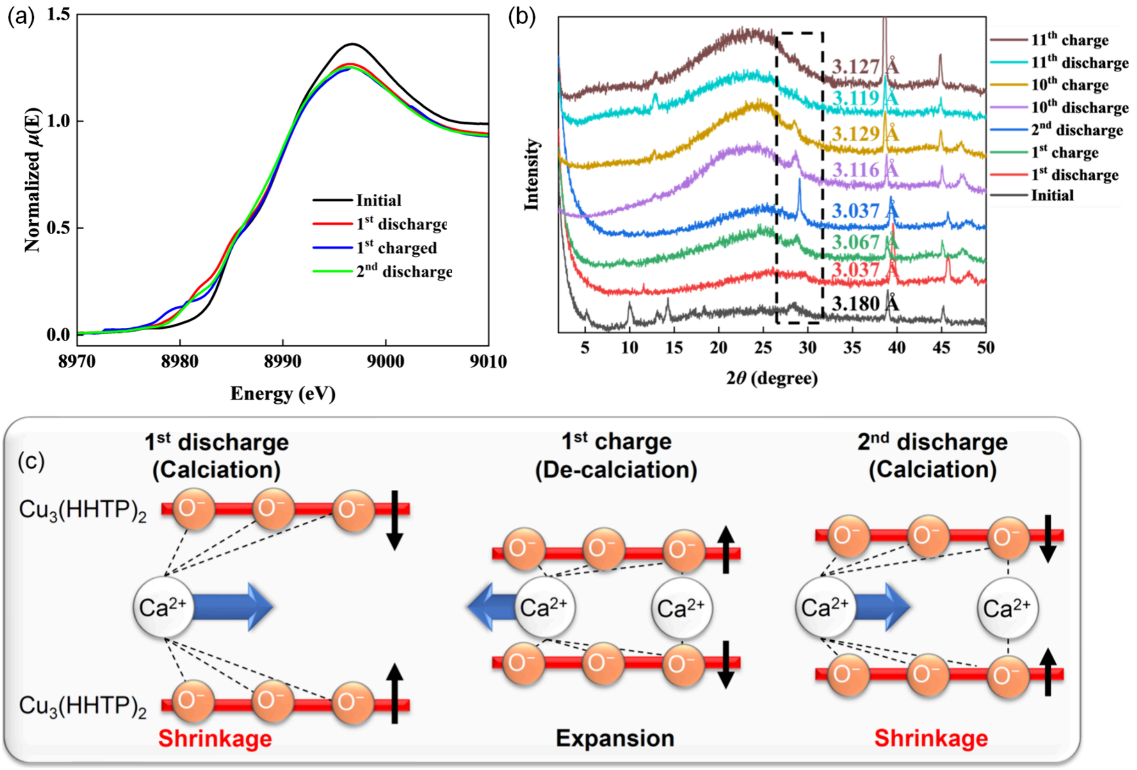

Figure 4. (a) Operando XANES spectra of the $Cu_3(HHTP)_2$ cathode in a CIB. (b) Ex situ PXRD patterns of the $Cu_3(HHTP)_2$ cathode in the initial (black), first discharge (red), first charge (green), and second discharge (blue), 10th charge (purple), and 10th discharge (ocher) states. (c) Proposed mechanism of calciation into and de-calciation from $Cu_3(HHTP)_2$ in the first discharge, first charge, and second discharge states.

that in the initial state, resulting in insufficient de-calciation during charging. We believe that de-calciation can be enhanced by using cathode active materials with a three-dimensional crystal structure to avoid shrinkage of the space for accommodation of Ca^{2+}.[40] The findings of this study will pave the way for the development of promising cathode active materials for CIBs.

■ EXPERIMENTAL SECTION

Preparation of $Cu_3(HHTP)_2$

All reagents were used without further purification. $Cu_3(HHTP)_2$ was prepared using a modified version of a synthetic method reported in the literature.[37] First, 2,3,6,7,10,11-hexahydroxytriphenylene (HHTP, $C_{18}H_{12}O_6$; 7.18×10^{-1} mmol; Tokyo Chemical Industry) was added to a mixture of distilled water (24 mL) and *N*,*N*-dimethylformamide (3 mL) in a flask (solution A). Meanwhile, copper(II) sulfate pentahydrate ($CuSO_4 \bullet 5H_2O$, 1.64 mmol) was added to distilled water (9 mL) in another flask (solution B). Solutions A and B were heated and stirred in an oil bath at 80 °C for 5 min. Subsequently, solution B was added to solution A, and the mixture was heated and stirred in an oil bath at 80°C for 12 h. A dark-blue solid precipitated in solution and was separated by centrifugation (Sigma 3-16L, Kubota) at 10,000 rpm for 1 h. The supernatant liquid was filtered, and the precipitate was washed three times each with distilled water, ethanol, and acetone. Finally, the wet solid was dried under vacuum overnight at room temperature (approximately 30 °C) to obtain $Cu_3(HHTP)_2$ as a dark blue powder.

Characterization

The powder X-ray diffraction (PXRD) patterns of $Cu_3(HHTP)_2$ were recorded using a MiniFlex 600 X-ray diffractometer (Rigaku) equipped with a Cu-target tube operated at 40 kV and 15 mA. The sample was ground into powder, and diffraction data were collected at 2θ angles of 2−50° using Cu K_α radiation.

Scanning electron microscopy (SEM) images were taken using a Miniscope TM1000 scanning electron microscope (Hitachi Hi-Tech) with the voltage set to 15 kV. $Cu_3(HHTP)_2$ on carbon tape was sputtered with gold in vacuo, and then SEM images of the sample were taken under high vacuum.

Fabrication of Thin-Film Cathode and Pellet Anode

The thin-film cathode was fabricated as follows: First, $Cu_3(HHTP)_2$ was added to carbon black (Toka Black 5500, Tokai carbon) and ground in an agate mortar for 40 min. Subsequently, a carboxy methyl cellulose (CMC) binder (Wako) was added, and the mixture was ground for 40 min. The weight ratio of $Cu_3(HHTP)_2$, carbon black, and CMC in the mixture was 30:60:10. The mixture was stirred in *N*-methylpyrrolidone (NMP), and the prepared slurry was uniformly coated (at approximately 100 μm) onto an aluminum foil with a thickness of 20 μm using the doctor blade technique and dried overnight under vacuum at room temperature. The foil was cut into a disc with a diameter of 15.95 mm. The pellet anode was fabricated as follows: First, carbon black (Toka Black 5500) and polyacrylonitrile (PAN) were ground in an agate mortar for 40 min. The weight ratio of carbon black and PAN in the mixture was 80:20. Subsequently, the mixture was stirred in NMP, and the prepared slurry was uniformly spread onto a polypropylene sheet, cut into a disc with a diameter of 17.00 mm (due to shrinkage after drying), and then dried overnight.

Battery Assembly

CR2032 coin-type cells were assembled using the thin-film cathode, pellet anode, glass microfiber filter separator (Whatman®, grade GF/A, φ = 17.00 mm), and 0.45 M $Ca(BF_4)_2$ (Thermo Fisher Scientific) in ethylene carbonate/propylene carbonate (EC/PC, 1/1 v/v; Tokyo Chemical Industry) in an Ar-filled glovebox.

Electrochemical Measurements

Cyclic voltammetry (CV) measurements of the CR2032 coin-type cells were performed at room temperature (approximately 293 K) using an HZ-Pro S12 multi-electrochemical measurement system (Hokuto Denko). A sweep rate and voltage range of 10 mV s^{-1} and

−1.0−1.5 V, respectively, were used to easily detect the redox reactions of the Cu ion and organic linker HHTP in the metal−organic framework.

Galvanostatic charge/discharge measurements of the calcium-ion batteries (CIBs) with a $Cu_3(HHTP)_2$ thin-film cathode were conducted at room temperature using an HJ1020mSD8 charging/discharging device (Hokuto Denko). The current density and voltage range were set to 100 mA g^{-1} and −1.0−1.5 V (vs. activated carbon, AC), respectively. In addition, the voltage vs. AC was converted into that versus Ca/Ca^{2+}, based on the previous study.[41] We constructed a three-electrode cell with Pt as the working electrode (WE), AC as the counter and reference electrodes (CE and RE, respectively), and a 0.45 M $Ca(BF_4)_2$ in EC:PC electrolyte with 0.05 M ferrocene (Fc) added. We performed CV measurements with a voltage range of −1.0 to +1.0 V and a scan rate of 10 mV/s. For comparison, we also created a cell with the same electrolyte (0.45 M $Ca(BF_4)_2$ in EC:PC) without adding Fc and performed CV measurements under the same conditions. In Figure S7a, oxidation and reduction peaks of Fc/Fc^+ were observed at 0.2000 and −0.1904 V, respectively. This is confirmed by the absence of peaks in Figure S7b where Fc is not added, further supporting that the peaks correspond to Fc/ferrocenium (Fc^+). The redox potential was calculated as a half wave potential of reduction and oxidation voltages, and to be 0.0048 V vs AC. Given that the redox potential of Fc/Fc^+ is 0.4 V vs standard hydrogen electrode (SHE)[42] and that of Ca/Ca^{2+} is −2.87 V vs SHE,[43] the conversion from vs AC to vs Ca/Ca^{2+} would require a shift of +3.2652 V. It is important to note that this vs AC value also includes the electrolyte dependence, which, in this system, incorporates the contribution of $Ca(BF_4)_2$ in EC:PC.

Elucidation of Reaction Mechanism

To investigate the electrochemical reaction mechanism of $Cu_3(HHTP)_2$, pellet cathodes were fabricated as follows. A paste was prepared by adding NMP to a ground mixture containing 30 wt % $Cu_3(HHTP)_2$, 60 wt % carbon black, and 10 wt % CMC in a mortar. The paste was uniformly spread onto a polypropylene sheet, which was then cut into discs with a diameter of 15.95 mm and dried overnight.

For operando X-ray absorption fine structure (XAFS) measurements, a battery with a Kapton film as an X-ray window[44] was fabricated using the $Cu_3(HHTP)_2$ pellet cathode, carbon pellet anode, 0.45 M $Ca(BF_4)_2$ in EC/PC (1/1, v/v) electrolyte, and glass microfiber filter separator (grade GF/A). Operando Cu K-edge XAFS measurements were conducted in transmission mode at room temperature using the BL14B1 beamline at SPring-8, Japan (8.0 GeV, 100 mA). An operando battery was placed between the two transmission ion chambers. X-rays from a bending magnet were monochromatized using a Si(111) double-crystal monochromator. The intensities of the incident (I_0) and transmitted (I_1) X-rays were detected using ion chambers filled with N_2 (100 %, I_0 chamber) or N_2/Ar (75/25, I_1 chamber). The X-ray spot size at the measurement position was adjusted horizontally and vertically to 1.0 and 0.8 mm, respectively, using a slit. The average valence of Cu in $Cu_3(HHTP)_2$ was calculated using the intensity of the pre-edge in the Cu K-edge X-ray absorption near edge structure (XANES) spectrum of a Cu_2O standard material with BN.

Ex situ PXRD measurements were performed using a MiniFlex 600 X-ray diffractometer (Rigaku) equipped with a Cu-target tube operated at 40 kV and 15 mA. CR2032 coin-type batteries [cathode: $Cu_3(HHTP)_2$ pellet cathode; anode: carbon pellet anode; electrolyte: 0.45 M $Ca(BF_4)_2$ in EC/PC (1/1, v/v); separator: glass microfiber filter (grade GF/A)] were maintained at −1.0 and 1.5 V during discharging and charging, respectively. After opening the circuits, the batteries were disassembled in air, and the $Cu_3(HHTP)_2$ pellet cathodes were dried overnight. Samples for PXRD measurements were prepared by grinding the cathodes, and data were collected at 2θ angles of 5−50° using Cu K_α radiation.

Ex situ energy-dispersive X-ray spectroscopy mapping analysis was performed using a MiniFlex 600 X-ray diffractometer (Rigaku). The discharged and charged $Cu_3(HHTP)_2$ pellet cathodes were obtained using the same methods as that for the ex situ PXRD measurements. The cathodes were washed once with PC, and then the ratio of Ca to Cu in each state (initial, first discharge, first charge, and second discharge) was determined.

Ex situ inductively coupled plasma-mass spectroscopy (ICP-MS) measurement was performed using a plasma atomic emission spectrometer (ICPE-9000, Shimadzu). The discharged and charged $Cu_3(HHTP)_2$ pellet cathodes were obtained using the same methods as that for the ex situ PXRD measurements. The cathodes were washed once with PC, and then 10 ppm of copper solution was prepared using cathodes and 2% HNO_3. In addition, 100 mL of x ppm of Ca + Cu in 2% HNO_3 (x = 0, 1, 10, 100) were used as standard solution. The ratio of Ca to Cu in each state (initial, first discharge, first charge, and second discharge) was plotted.

■ ASSOCIATED CONTENT

Supporting Information

The Supporting Information is available free of charge at https://pubs.acs.org/doi/10.1021/acselectrochem.5c00241.

> Experimental details, SEM image of as-prepared $Cu_3(HHTP)_2$, analytical data of $Cu_3(HHTP)_2$ during the discharge−charge processes, battery performance list of $Cu_3(HHTP)_2$, and metal-oxide-based cathode active materials (PDF)

■ AUTHOR INFORMATION

Corresponding Authors

Hirofumi Yoshikawa − *School of Engineering, Kwansei Gakuin University, Sanda, Hyogo 669-1337, Japan;* orcid.org/0000-0002-0088-1579; Email: yoshikawah@kwansei.ac.jp

Takeshi Shimizu − *Chemistry and Biochemistry Division, National Institute of Technology, Yonago College, Yonago, Tottori 683-8502, Japan;* orcid.org/0000-0003-3817-7154; Email: t-shimizu@yonago-k.ac.jp

Authors

Katsuhiro Wakamatsu − *School of Engineering, Kwansei Gakuin University, Sanda, Hyogo 669-1337, Japan;* orcid.org/0000-0003-0682-453X

Shunsuke Ohkata − *School of Engineering, Kwansei Gakuin University, Sanda, Hyogo 669-1337, Japan*

Mizuki Kajiwara − *Chemistry and Biochemistry Division, National Institute of Technology, Yonago College, Yonago, Tottori 683-8502, Japan*

Naoki Tanifuji − *Chemistry and Biochemistry Division, National Institute of Technology, Yonago College, Yonago, Tottori 683-8502, Japan*

Complete contact information is available at: https://pubs.acs.org/10.1021/acselectrochem.5c00241

Author Contributions

‡K.W. and S.O. contributed equally.

Notes

The authors declare no competing financial interest.

■ ACKNOWLEDGMENTS

This work was financially supported by the Japan Society for the Promotion of Science KAKENHI (Grant Nos. JP 26288091, 23550169, 21K14727, 19K22222, 20H04680, and 20H04646 for H.Y.; 21K14727 for T.S.; and 26288091 and 23550169 for N.T.), Mazda Foundation Research Grants

(Research Foundation for the Electrotechnology of Chubu and Electric Technology Research Foundation of Chugoku for T.S. and Electric Technology Research Foundation of Chugoku for N.T.), and the GEAR 5.0 Project of the National Institute of Technology (KOSEN), Japan. Synchrotron radiation experiments for Cu K-edge XAFS spectroscopy were performed at beamlines BL14B1, BL14B2, and BL27SU of SPring-8, Japan Atomic Energy Agency (JAEA), with the approval of the Japan Synchrotron Radiation Research Institute (JASRI) (Proposal Nos. 2023A3634 and 2023B3634 for BL14B1, 2024A1738, 2024B1892, 2025B1654, and 2025B2140 for BL14B2 and 2024A1086 for BL27SU). These experiments were also performed under the Shared Use Program of JAEA Facilities (Proposal Nos. 2023A-E01 and 2023B-E01) with the approval of the Advanced Research Infrastructure for Materials (ARIM) (Proposal Nos. JPMXP1223AE0001 and JPMXP1223AE0018) projects supported by the Ministry of Education, Culture, Sports, Science, and Technology (MEXT), Japan. We also thank Editage (www.editage.com) for the English language editing.

■ REFERENCES

(1) Reddy, M. V.; Mauger, A.; Julien, C. M.; Paolella, A.; Zaghib, K. Brief History of Early Lithium-Battery Development. *Materials* **2020**, *13*, 1884.

(2) Goodenough, J. B.; Park, K. S. The Li-Ion Rechargeable Battery: A Perspective. *J. Am. Chem. Soc.* **2013**, *135*, 1167−1176.

(3) Wu, Y.; Shuang, W.; Wang, Y.; Chen, F.; Tang, S.; Wu, X. L.; Bai, Z.; Yang, L.; Zhang, J. Recent Progress in Sodium-Ion Batteries: Advanced Materials, Reaction Mechanisms and Energy Applications. *Electrochem. Energy Rev.* **2024**, *7*, 17.

(4) Bai, Y.; Zhang, H.; Liang, W.; Zhu, C.; Yan, L.; Li, C. Advances of Zn Metal-Free "Rocking-Chair"-Type Zinc Ion Batteries: Recent Developments and Future Perspectives. *Small* **2024**, *20*, No. 2306111.

(5) Ji, B.; He, H.; Yao, W.; Tang, Y. Recent Advances and Perspectives on Calcium-Ion Storage: Key Materials and Devices. *Adv. Mater.* **2021**, *33*, No. 2005501.

(6) Gummow, R. J.; Vamvounis, G.; Kannan, M. B.; He, Y. Calcium-Ion Batteries: Current State-of-the-Art and Future Perspectives. *Adv. Mater.* **2018**, *30*, No. 1801702.

(7) Sheng, D.; Liu, X.; Zhang, Q.; Yi, H.; Wang, X.; Fu, S.; Zhou, S.; Shen, J.; Gao, A. Intercalation Reaction of Molybdenum Trioxide Cathode for Rechargeable Ion Batteries. *Batteries Supercaps* **2023**, *6*, No. e202200569.

(8) Shannon, R. D. Revised Effective Ionic Radii and Systematic Studies of Interatomic Distances in Halides and Chalcogenides. *Acta Crystallogr.* **1976**, *A32*, 751.

(9) Liu, Z.; Qin, L.; Cao, X.; Zhou, J.; Pan, A.; Fang, G.; Wang, S.; Liang, S. Ion Migration and Defect Effect of Electrode Materials in Multivalent-Ion Batteries. *Prog. Mater. Sci.* **2022**, *125*, No. 100911.

(10) Chando, P. A.; Chen, S.; Shellhamer, J. M.; Wall, E.; Wang, X.; Schuarca, R.; Smeu, M.; Hosein, I. D. Exploring Calcium Manganese Oxide as a Promising Cathode Material for Calcium-Ion Batteries. *Chem. Mater.* **2023**, *35*, 8371−8381.

(11) Cabello, M.; Nacimiento, F.; González, J. R.; Ortiz, G.; Alcántara, R.; Lavela, P.; Pérez-Vicente, C.; Tirado, J. L. Advancing towards a Veritable Calcium-Ion Battery: $CaCo_2O_4$ Positive Electrode Material. *Electrochem. Commun.* **2016**, *67*, 59−64.

(12) Xu, X.; Duan, M.; Yue, Y.; Li, Q.; Zhang, X.; Wu, L.; Wu, P.; Song, B.; Mai, L. Bilayered $Mg_{0.25}V_2O_5{\cdot}H_2O$ as a Stable Cathode for Rechargeable Ca-Ion Batteries. *ACS Energy Lett.* **2019**, *4*, 1328−1335.

(13) Arroyo-de Dompablo, M. E.; Krich, C.; Nava-Avendaño, J.; Palacín, M. R.; Bardé, F. In Quest of Cathode Materials for Ca Ion Batteries: The $CaMO_3$ Perovskites (M = Mo, Cr, Mn, Fe, Co, and Ni). *Phys. Chem. Chem. Phys.* **2016**, *18*, 19966−19972.

(14) Park, H.; Cui, Y.; Kim, S.; Vaughey, J. T.; Zapol, P. Ca Cobaltites as Potential Cathode Materials for Rechargeable Ca-Ion Batteries: Theory and Experiment. *J. Phys. Chem. C* **2020**, *124*, 5902−5909.

(15) Cabello, M.; Nacimiento, F.; Alcántara, R.; Lavela, P.; Pérez Vicente, C.; Tirado, J. L. Applicability of Molybdite as an Electrode Material in Calcium Batteries: A Structural Study of Layer-type Ca_xMoO_3. *Chem. Mater.* **2018**, *30*, 5853−5861.

(16) Carrasco, J. Role of van der Waals Forces in Thermodynamics and Kinetics of Layered Transition Metal Oxide Electrodes: Alkali and Alkaline-Earth Ion Insertion into V_2O_5. *J. Phys. Chem. C* **2014**, *118*, 19599−19607.

(17) Wang, J.; Tan, S.; Xiong, F.; Yu, R.; Wu, P.; Cui, L.; An, Q. $VOPO_4{\cdot}2H_2O$ as a New Cathode Material for Rechargeable Ca-Ion Batteries. *Chem. Commun.* **2020**, *56*, 3805−3808.

(18) Murata, Y.; Inada, R.; Sakurai, Y. Electrolyte Dependency on Ca^{2+} Insertion and Extraction Properties of V_2O_5. *J. Electrochem. Soc.* **2021**, *168*, No. 020528.

(19) Xu, Z. L.; Park, J.; Wang, J.; Moon, H.; Yoon, G.; Lim, J.; Ko, Y. J.; Cho, S. P.; Lee, S. Y.; Kang, K. A new high-voltage calcium intercalation host for ultra-stable and high-power calcium rechargeable batteries. *Nat. Commun.* **2021**, *12*, 3369.

(20) Li, R.; Lee, Y.; Lin, H.; Che, X.; Pu, X.; Yi, Y.; Chen, F.; Yu, J.; Chan, K. C.; Park, K.; Xu, Z. K_xVPO_4F (x~0): A New High-Voltage and Low-Stain Cathode Material for Ultrastable Calcium Rechargeable Batteries. *Adv. Energy Mater.* **2024**, *14*, No. 2302700.

(21) Ma, Y.; Qi, Q.; Meng, Q.; Yi, Y.; Lin, H.; Yu, J.; Cheung, C. F.; Xu, Z. A Small Molecular Cathode for High-Performance Calcium Metal Batteries. *Adv. Funct. Mater.* **2025**, *35*, No. 2411715.

(22) Liu, J.; Xie, D.; Shi, W.; Cheng, P. Coordination Compounds in Lithium Storage and Lithium-Ion Transport. *Chem. Soc. Rev.* **2020**, *49*, 1624−1642.

(23) Férey, G.; Millange, F.; Morcrette, M.; Serre, C.; Doublet, M.-L.; Grenèche, J.-M.; Tarascon, J.-M. Mixed-Valence Li/Fe-Based Metal−Organic Frameworks with Both Reversible Redox and Sorption Properties. *Angew. Chem. Int. Ed.* **2007**, *46*, 3259−3263.

(24) Zhang, Z.; Yoshikawa, H.; Awaga, K. Monitoring the Solid-State Electrochemistry of Cu(2,7-AQDC) (AQDC = Anthraquinone Dicarboxylate) in a Lithium Battery: Coexistence of Metal and Ligand Redox Activities in a Metal−Organic Framework. *J. Am. Chem. Soc.* **2014**, *136*, 16112−16115.

(25) Liu, Z.; Zheng, F.; Xiong, W.; Li, X.; Yuan, A.; Pang, H. Strategies to Improve Electrochemical Performances of Pristine Metal-Organic Frameworks-Based Electrodes for Lithium/Sodium-Ion Batteries. *SmartMat* **2021**, *2*, 488−518.

(26) Wang, Z.; Tao, H.; Yue, Y. Metal-Organic-Framework-Based Cathodes for Enhancing the Electrochemical Performances of Batteries: A Review. *ChemElectroChem.* **2019**, *6*, 5358−5374.

(27) Ma, Y.; Ma, Y.; Dreyer, S. L.; Wang, Q.; Wang, K.; Goonetilleke, D.; Omar, A.; Mikhailova, D.; Hahn, H.; Breitung, B.; Brezesinski, T. High-Entropy Metal−Organic Frameworks for Highly Reversible Sodium Storage. *Adv. Mater.* **2021**, 33, No. 2101342.

(28) Shimizu, T.; Mameuda, T.; Toshima, H.; Akiyoshi, R.; Kamakura, Y.; Wakamatsu, K.; Tanaka, D.; Yoshikawa, H. Application of Porous Coordination Polymer Containing Aromatic Azo Linkers as Cathode-Active Materials in Sodium-Ion Batteries. *ACS Appl. Energy Mater.* **2022**, *5*, 5191−5198.

(29) Yoshida, Y.; Kato, K.; Sadakiyo, M. Vapor-Induced Superionic Conduction of Magnesium Ions in a Metal−Organic Framework. *J. Phys. Chem. C* **2021**, *125*, 21124−21130.

(30) Yoshida, Y.; Yamada, T.; Jing, Y.; Toyao, T.; Shimizu, K.; Sadakiyo, M. Super Mg^{2+} Conductivity around 10^{-3} S cm^{-1} Observed in a Porous Metal−Organic Framework. *J. Am. Chem. Soc.* **2022**, *144*, 8669−8675.

(31) Niwa, S.; Sadakiyo, M. Preparation of a Mg^{2+}-Containing MOF through Ion Exchange and Its High Ionic Conductivity. *Dalton Trans.* **2022**, *51*, 12037−12040.

(32) Nobakht, N.; Etghani, S. A.; Hosseini, M.; Aboutalebi, S. H. Two-Dimensional MOF-Based Materials: Preparations and Applications as Electrodes in Li-Ion Batteries. *J. Energy Chem.* **2024**, *97*, 388−418.

(33) Amores, M.; Wada, K.; Sakaushi, K.; Nishihara, H. Reversible Energy Storage in Layered Copper-Based Coordination Polymers: Unveiling the Influence of the Ligand's Functional Group on Their Electrochemical Properties. *J. Phys. Chem. C* **2020**, *124*, 9215−9224.

(34) Jiang, Q.; Xiong, P.; Liu, J.; Xie, Z.; Wang, Q.; Yang, X.-Q.; Hu, E.; Cao, Y.; Sun, J.; Xu, Y.; Chen, L. A Redox-Active 2D Metal−Organic Framework for Efficient Lithium Storage with Extraordinary High Capacity. *Angew. Chem. Int. Ed.* **2020**, *59*, 5273−5277.

(35) Nam, K. W.; Park, S. S.; dos Reis, R.; Dravid, V. P.; Kim, H.; Mirkin, C. A.; Stoddart, J. F. Conductive 2D Metal-Organic Framework for High-Performance Cathodes in Aqueous Rechargeable Zinc Batteries. *Nat. Commun.* **2019**, *10*, 4948.

(36) Wrogemann, J. M.; Lüther, M. J.; Bärmann, P.; Lounasvuori, M.; Javed, A.; Tiemann, M.; Golnak, R.; Xiao, J.; Petit, T.; Placke, T.; Winter, M. Overcoming Diffusion Limitation of Faradaic Processes: Property-Performance Relationships of 2D Conductive Metal-Organic Framework $Cu_3(HHTP)_2$ for Reversible Lithium-Ion Storage. *Angew. Chem. Int. Ed.* **2023**, *62*, No. e202116668.

(37) Day, R. W.; Bediako, D. K.; Rezaee, M.; Parent, L. R.; Skorupskii, G.; Arguilla, M. Q.; Hendon, C. H.; Stassen, I.; Gianneschi, N. C.; Kim, P.; Dincă, M. Single Crystals of Electrically Conductive Two-Dimensional Metal−Organic Frameworks: Structural and Electrical Transport Properties. *ACS Cent. Sci.* **2019**, *5*, 1959−1964.

(38) Li, J.; Han, C.; Ou, X.; Tang, Y. Concentrated Electrolyte for High-Performance Ca-Ion Battery Based on Organic Anode and Graphite Cathode. *Angew. Chem. Int. Ed.* **2022**, *61*, No. e202116668.

(39) Lamberti, C.; Bordiga, S.; Bonino, F.; Prestipino, C.; Berlier, G.; Capello, L.; D'Acapito, F.; Llabrés i Xamena, F. X.; Zecchina, A. Determination of the Oxidation and Coordination State of Copper on Different Cu-Based Catalysts by XANES Spectroscopy *In Situ* or in *Operando* Conditions. *Phys. Chem. Chem. Phys.* **2003**, *5*, 4502−4509.

(40) Tojo, T.; Sugiura, Y.; Inada, R.; Sakurai, Y. Reversible Calcium Ion Batteries Using a Dehydrated Prussian Blue Analogue Cathode. *Electrochim. Acta* **2016**, *207*, 22−27.

(41) Nishimura, Y.; Yamazaki, S.; Sakoda, T.; Nakagawa, K. Investigation of the electrochemical intercalation of Ca^{2+} into graphite layer carbon nano filaments as a novel electrode material for calcium-ion batteries. *SN Appl. Sci.* **2023**, *5*, 58.

(42) Dorčák, V.; Hrbáč, J.; Janata, J.; Vacek, J. Metallocene Voltammetric Reference Related to a Normal Hydrogen Electrode. *J. Phys. Chem. Lett.* **2025**, *16*, 2487−2491.

(43) Deng, X.; Li, L.; Zhang, G.; Zhao, X.; Hao, J.; Han, C.; Li, B. Anode chemistry in calcium ion batteries: A review. *Energy Storage Mater.* **2022**, *53*, 467−481.

(44) Wang, H.; Hamanaka, S.; Yokoyama, T.; Yoshikawa, H.; Awaga, K. In-situ XAFS Studies of Mn12 Molecular-Cluster Batteries: Super-Reduced Mn12 Clusters in Solid-State Electrochemistry. *Chem.—Asian J.* **2011**, *6*, 1074−1079.